STRUCTURAL CHEMISTRY

ISSN 2053-2296

Molecular simulation of imperfect structure I CO_2 hydrate growth in brine

Ziyi Fu,[a]* Xianwu Jing,[a,b]* Li Zhou,[a] Qin Luo[a] and Pengfei Zhang[a]

[a]Research Institute of Natural Gas Technology, PetroChina Southwest Oil and Gasfield Company, Chengdu, Sichuan 610213, People's Republic of China, and [b]Shale Gas Evaluation and Exploitation Key Laboratory of Sichuan Province, Sichuan Provincial Department of Science and Technology, Chengdu, Sichuan 610051, People's Republic of China. *Correspondence e-mail: fuziyi@petrochina.com.cn, jingxw2018@petrochina.com.cn

Received 3 August 2023
Accepted 22 November 2023

Edited by R. Diniz, Universidade Federal de Minas Gerais, Brazil

Keywords: CO_2 hydrate; molecular dynamics simulation; order parameters; climate change; IPCC; carbon capture.

In order to investigate the viability of carbon dioxide (CO_2) storage in seawater, molecular dynamics techniques were employed to study the dynamic evolution of CO_2 hydrate in saline water. The simulation was conducted under specific conditions: a temperature of 275 K, a pressure of 10 MPa and a simulated marine environment achieved using a 3.4 wt% sodium chloride (NaCl) solution. The total simulation time was 1000 ns. The results of the simulation indicate that the pre-existence of CO_2 hydrate crystals as seeds leads to rapid growth of CO_2 hydrate. However, analysis of the F3 and F4 order parameters reveals that the hydrate does not meet the standard values of the perfect structure I (sI) type, confirming the existence of an imperfect structure during the simulation. Additionally, the changes in the number of different phase states of water molecules during the hydrate growth process shows that there are always some liquid water molecules, which means some water molecules fail to form solid water cages. Further investigation suggests that the presence of Na^+ and Cl^- hampers the hydrogen bonds between water molecules, resulting in incomplete cage structures. By analyzing the density variations in the system, it is observed that CO_2 hydrate, with a density of around 1.133 g cm^{-3}, forms rapidly, surpassing the average density of seawater. This density increase facilitates the efficient and swift containment of CO_2 on the seabed, thereby supporting the feasibility of the CO_2 storage theory.

1. Introduction

Greenhouse gases, primarily generated by human activities and the burning of fossil fuels, contribute significantly to climate change. The most common way people perceive climate change is through extreme weather events, and we are now witnessing the emergence of high-temperature conditions that surpass what humans can tolerate (Raymond *et al.*, 2020). Since 1950, there has been a notable increase in the frequency and intensity of extreme high temperatures, including heatwaves, in many parts of the world. Studies have shown that the severity of heatwaves, including temperature, duration and extent of impact, is steadily rising in correlation with global warming (Wang & Yan, 2021). The sixth Intergovernmental Panel on Climate Change (IPCC) report (Arias *et al.*, 2021) confirms that human activities have significantly contributed to rising temperatures in the atmosphere, oceans and land surfaces, resulting in an unprecedented rate of warming over the past two millennia. The primary cause of global warming is the release of greenhouse gases, such as CO_2, and existing models predict that global greenhouse gas emissions must peak between 2020 and 2025 (at the latest) if we want to limit the warming of the Earth to within 2 °C (Rogelj *et al.*, 2016; McGlade & Ekins, 2015).

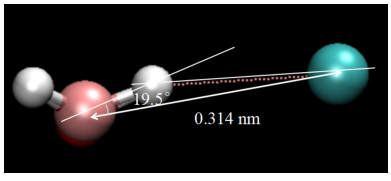

The consequences of climate change are already evident in the accelerated melting of glaciers (Hugonnet *et al.*, 2021), recurring mountain fires (Canadell *et al.*, 2021) and rising sea levels (Dangendorf *et al.*, 2023). It is crucial to recognize the urgent and imperative need to address these climate challenges. As a response, the European Union and the G8 have set a target to reduce greenhouse gas emissions by at least 80% from the 1990 levels by 2050 (Viebahn *et al.*, 2015; Faure-Schuyer *et al.*, 2017). Scientists are actively exploring new technologies to help achieve the goal of carbon neutrality, and Carbon Capture and Storage (CCS) is considered a crucial strategy for decarbonizing the power and industrial sectors (Turgut *et al.*, 2021). The final step in the CCS process is the permanent sequestration of CO_2, which can be accomplished through various approaches, such as mineral carbonation, oceanic storage and underground geological storage (Aminu *et al.*, 2017). Storing CO_2 in the form of hydrate on the seabed is particularly promising and an area of active research. CO_2 hydrate is a crystal-like structure that has a nonstoichiometric composition, consisting of cages that resemble a three-dimensional lattice (Aya *et al.*, 1997). At a microscopic level, these cages are formed by water molecules bonded together through hydrogen bonds, and they can trap guest molecules such as methane (CH_4) and CO_2. The water cages are composed of interconnected rings of hydrogen-bonded water molecules, with five- and six-membered rings being common. Different types of crystalline structures can be formed through these interconnected rings (Jing *et al.*, 2022; Walsh *et al.*, 2009).

CO_2 hydrate and CH_4 hydrate have typically the sI-type structure, which includes two types of cages: 5^{12} and $5^{12}6^2$ (Koh, 2002; Kirchner *et al.*, 2004). CO_2 hydrate has a higher density than seawater, making it stable on the surface of the seabed and near seabed sediments. They can store large amounts of CO_2 with high gas storage density and exhibit good mechanical stability. As a result, CO_2 hydrate is considered to have significant potential for safe, long-term and stable storage of CO_2, offering broad applications (Zheng *et al.*, 2020). Therefore, it is crucial to understand the growth of CO_2 hydrate in seawater. Molecular dynamics simulation is a valuable technique for investigating CO_2 hydrate, offering a systematic understanding of the microscopic evolution at the molecular/atomic scale. This approach enhances the efficiency and predictability of our research. In a study by He *et al.* (2017), comprehensive microsecond simulations were conducted to explore the nucleation of CO_2 hydrate. The findings indicate a close relationship between nucleation and the hydration shells of CO_2 in water. The adsorption of CO_2 molecules around the hydration shell significantly stabilizes the hydrogen bonds within it and facilitates the transformation of the hydration shell into a cage structure. Zhang *et al.* (2019) utilized molecular dynamics simulation to establish a model for CO_2 hydrate formation. This model enabled the observation of water and CO_2 molecule movements in various systems with different initial conditions. Their research primarily focused on assessing the impact of temperature on CO_2 generation (Zhang *et al.*, 2019). The results of Nakate *et al.* (2019) revealed that the concentration of CO_2 molecules in water plays a crucial role in growth kinetics. Maximizing the CO_2 concentration in the aqueous phase does not necessarily lead to faster growth of CO_2 hydrate. Interestingly, most studies focus on the nucleation process or the influence of external substances. When we talk about CO_2 storage, we more pay attention to the influence of major ions in seawater on the structure of hydrate and whether the structure of hydrate is perfect, in order to facilitate stable storage on the seabed.

In this article, we employed molecular dynamics methods to simulate the growth process of CO_2 hydrate in the marine

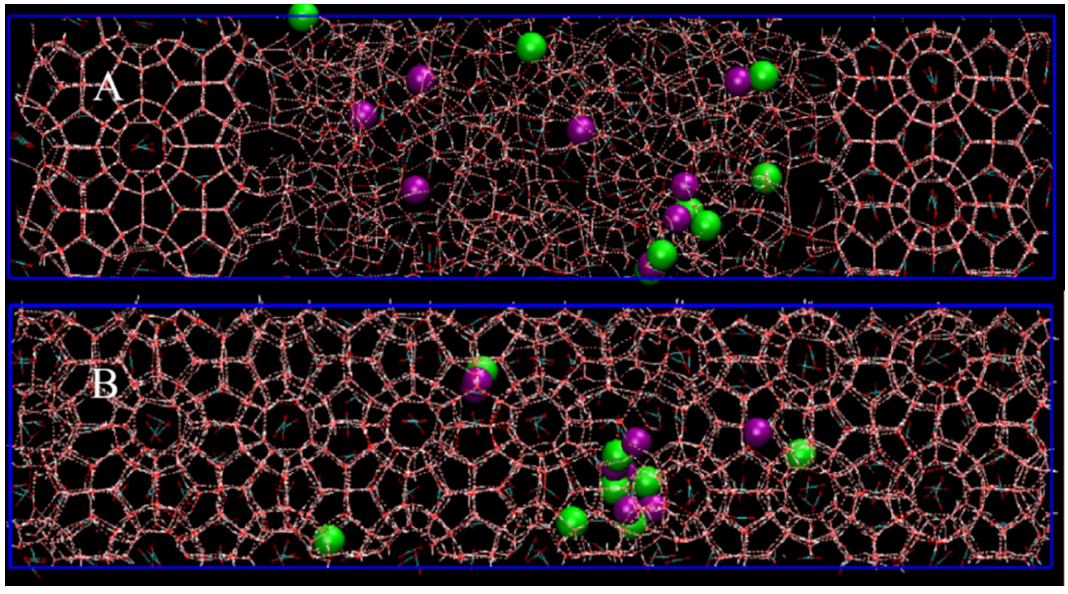

Figure 1
Simulation process of CO_2 hydrate growth, showing (A) the initial state, 0 ns, and (B) the final state, 1000 ns. The green balls represent Cl^- and the purple balls represent Na^+.

environment. Specifically, it analyzes the influence of NaCl on the cage structure of CO_2 hydrate and discusses variations in relevant parameters. The potential for storing CO_2 in seawater has also been discussed.

2. Computational details

Simulations were performed using *GROMACS* software (Version 2019.6; Abraham *et al.*, 2015; Van Der Spoel *et al.*, 2005). The growth process of CO_2 hydrate was studied from an sI-type CO_2 hydrate crystal seed. The results of the calculations were visualized using the software *VMD* (Visual Molecular Dynamics) (Version 1.9.3; Humphrey *et al.*, 1996). To examine the growth process of CO_2 hydrate, a $2 \times 2 \times 2$ supercell was constructed based on the structure described in a previous report (Izquierdo-Ruiz *et al.*, 2016) using *Multiwfn* software (Lu & Chen, 2012), with the lattice parameters $2.406 \times 2.406 \times 2.406$ nm. This supercell was then used as a seed to establish an initial box measuring $15 \times 2.5 \times 2.5$ nm, as shown in Fig. 1. The box contained two CO_2 hydrate seeds on both sides and CO_2 aqueous solution in the middle. 736 water molecules, 128 CO_2 molecules, 8 Na^+ cations and 8 Cl^- anions were placed within the middle aqueous solution, and the concentration of NaCl was about 3.4%, which is close to the concentration of NaCl in seawater. In this simulation, the TIP4P/Ice four-point water model (Abascal *et al.*, 2005) was adopted for the water molecule as it provides a more accurate representation of water near the freezing point. The EPM2 force field model was used for CO_2 (Harris & Yung, 1995), as it is widely employed in simulating CO_2 hydrate systems. The leap-frog integration algorithm with a time step of 2 fs was employed. The short-range nonbonded interactions between molecules were computed using the Lennard–Jones potential energy function, with a truncation distance of 1 nm. The long-range electrostatic interactions were computed using the Particle Mesh Ewald (PME) algorithm (Darden *et al.*, 1993). Periodic boundary conditions were applied in all directions, with only constraints applied to hydrogen bonds. The simulation was conducted under NPT (constant temperature and pressure) conditions, with the V-rescale algorithm (Bussi *et al.*, 2007) used for temperature control and the Parrinello–Rahman algorithm (Carretero-González *et al.*, 2005) used for pressure control. An anisotropic pressure coupling algorithm was employed and the total simulation time was 1000 ns. To mimic the simulation conditions as closely as possible, a 3.4% sodium chloride solution was utilized to represent a seawater environment with a temperature of 275 K and a pressure of 100 bar (1 bar = 10^5 Pa).

3. Results and discussion

3.1. CO_2 hydrate growth process

The formation of hydrate occurs when water molecules create cage-like structures by bonding with each other through hydrogen bonds, capturing gas molecules in the process. As

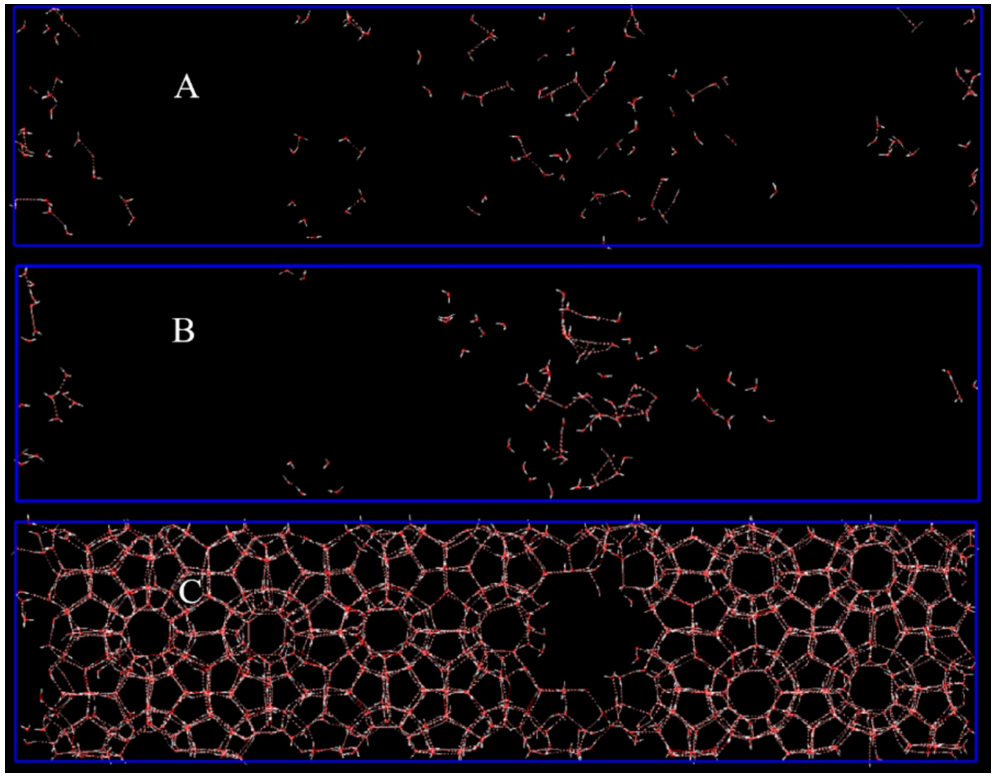

Figure 2
Water molecules belonging to different phase states, showing (A) water molecules at the interface between hydrate and liquid water, (B) water molecules belonging to liquid water and (C) water molecules belonging to hydrate.

the hydrate continues to develop, the number of cages increases and they stack together, leading to the consumption of free liquid water as it transforms into solid hydrate. In Fig. 1, the simulation depicting the growth of the hydrate system is clearly shown [part (A) represents the initial state at 0ns, while part (B) shows the end state at 1000 ns]. The visualization demonstrates how water molecules transition from a disordered arrangement to an ordered one, forming cage structures in which CO_2 gas is trapped.

However, the presence of Na^+ and Cl^- in the solution has a significant impact on the formation of CO_2 hydrate, resulting in substantial damage to the cage structure and the potential formation of imperfect hydrate. Thus, molecular dynamics simulations indicate that the growth of CO_2 hydrate in NaCl solution is inhibited, with NaCl actively impairing the cage structure and generating flawed hydrate.

Additionally, we conducted an analysis of defective areas and employed the CHILL+ algorithm (Nguyen & Molinero, 2015) to differentiate water molecules based on their respective phase states. Fig. 2 provides a characterization of water molecules in various phase states subsequent to hydrate formation. In Fig. 2(A), the water molecules are positioned between the liquid and solid states. In Fig. 2(B), liquid water molecules are illustrated, while Fig. 2(C) showcases water molecules in the hydrate state, forming 'cages' through hydrogen bonding. By examining the placement of Na^+ and Cl^- ions in Fig. 1, it is evident that an amorphous phase may occur as an interim stage before the transition to the crystalline phase. Within this region, both liquid water molecules and certain water molecules reside between the two phases. Fig. 2 demonstrates the perpetual existence of liquid water in the system, indicating that not all water molecules participate in the growth of hydrate cages, thereby resulting in defective hydrate.

3.2. Order parameters

Order parameters, also referred to as the three-body order parameter (F3) and the four-body order parameter (F4), are widely used parameters that describe the arrangement of water molecules (Jing *et al.*, 2022; Walsh *et al.*, 2009; Kirchner *et al.*, 2004).

For water molecules in different phase states, the F3 and F4 sequence parameters are different. F3 measures the extent to which the tetrahedron formed by the central O atom differs from a regular tetrahedron when considering other O atoms within a distance of 3.5 Å. The calculation formula for F3 is depicted in Equation (1). According to this definition, the F3 value for solid water (*e.g.* ice) and hydrate (both CH_4 hydrate and CO_2 hydrate) is 0.01, whereas the F3 value for liquid water is 0.1.

$$\mathrm{F3} = \frac{1}{n_i(n_i-1)} \sum_{j=1}^{n_i-1} \sum_{k=j+1}^{n_1} \left(\cos\theta_{jik} \mid \cos\theta_{jik} \mid + \cos^2(109.47^\circ)\right)^2 \quad (1)$$

In this context, θ symbolizes the angle formed by the O atom i in the central water molecule and the O atoms j and k in any two neighbouring water molecules within a 3.5 Å radius.

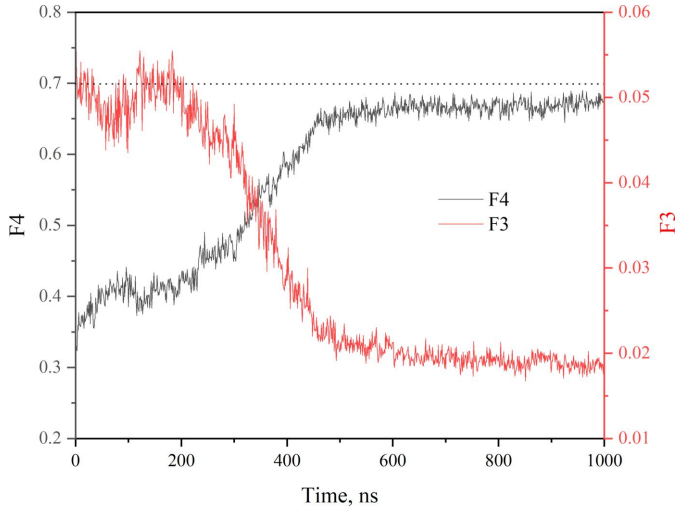

Figure 3
Changes of the F3 and F4 order parameters with simulation time.

The value of 109.47° corresponds to the angle between the central vertex line of a regular tetrahedron and represents the maximum value of the minimum angle among four vectors in three-dimensional space.

The value of F4 can be determined by computing the angle between the outermost H atom of two adjacent water molecules and the O atom within each water molecule. Equation (2) illustrates the specific formula for this calculation. The F4 parameter encompasses H-atom data and therefore provides an enhanced capability for discerning the structural characteristics of different solid forms of water. For instance, ice has an F4 value of −0.4, liquid water has an F4 value of −0.04 and the sI-type hydrate structure has an F4 value of 0.7.

$$\mathrm{F4} = \frac{1}{n_i} \sum_{i=1}^{n_i} \cos 3\phi_i \quad (2)$$

Fig. 3 illustrates the temporal variations of the F3 and F4 parameters. By examining the changes in the F3 order parameter, it is evident that they decrease during the simulation, implying a process of water molecule organization. The F3 order parameter values tend to approach 0.02, while the F4 parameter values tend to approach 0.7, deviating somewhat from the order parameter values reported in most literature for ideal CO_2 hydrate. The F4 order parameter exhibits a gradual increase until reaching its peak and then remains stable, indicating a rapid growth process for the CO_2 hydrate. However, it fails to meet the standard values of hydrate order parameters. For instance, Jing's study reported F4 parameter values of 0.74 and F3 parameter values of 0.01 for perfect CO_2 hydrate (Walsh *et al.*, 2009). This inconsistency could be attributed to interactions among Na^+, Cl^- and H_2O, which might hinder the participation of certain water molecules in the formation of complete cages or prevent the formation of specific cage types. Consequently, these factors affect the F3 and F4 parameters.

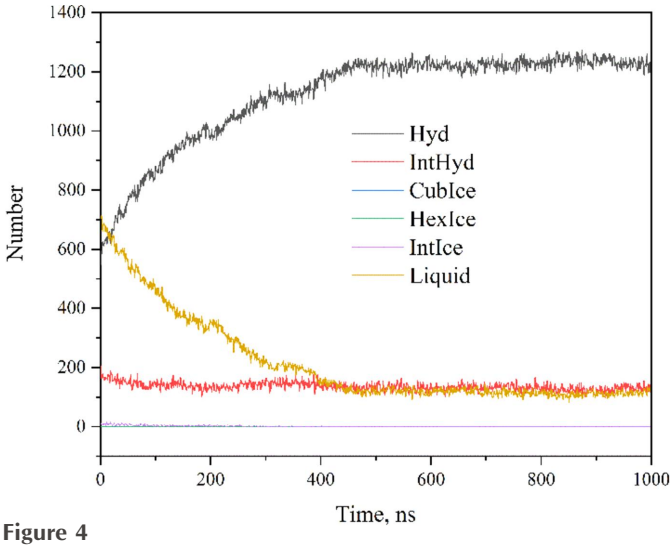

Figure 4
The number of different types of water molecules during the simulation process. 'Hyd' stands for water molecules belonging to the hydrate state, 'IntHyd' stands for water molecules at the interface between hydrate and liquid water, 'CubIce' stands for square ice molecules, 'HexIce' stands for hexagonal ice molecules, 'InterIce' stands for interface ice molecules and 'Liquid' stands for water molecules belonging to liquid water.

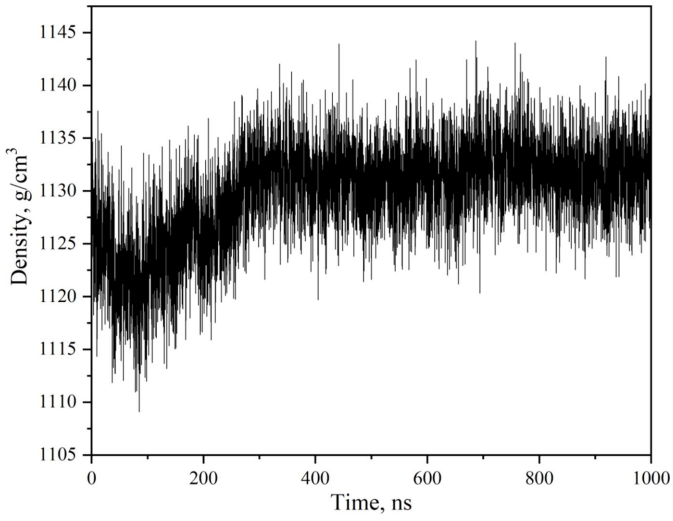

Figure 5
Density changes during the simulation process.

3.3. Number of different types of water molecules and density

To deeply analyze the growth and structural evolution of CO_2 hydrate in brine, we employed the CHILL+ algorithm (Nguyen & Molinero, 2015) to determine the quantities of water molecules associated with the hydrate, water molecules situated at the interface between the hydrate and the liquid phase, as well as liquid water molecules throughout the simulation. Fig. 4 illustrates the number of water molecules observed during the entire simulation. Within the time span of 0–500 ns, the number of water molecules attributed to hydrate increased rapidly from 600 to over 1200, indicating a significant generation of hydrate within the simulated system. Conversely, the count of water molecules in the liquid state experienced a sharp decline within the same time range, dropping from 700 to around 105. This decline further supports our previous analysis and highlights the substantial generation of hydrate during this time period. During the initial 0–500 ns, we observed a period of rapid growth in CO_2 hydrate, followed by a gradual slowdown leading to a stable state. Concurrently, the number of liquid water molecules decreased to approximately 100. This observation signifies the presence of free liquid water molecules in the simulated system, corroborating our earlier analysis. In the seawater system simulated with NaCl solution, the presence of Na^+ and Cl^- disrupted the cage structure, resulting in the formation of imperfect hydrate. Some liquid water molecules and water molecules between the two phases were found in regions enriched with Na^+ and Cl^-. Throughout the simulation, the quantity of water molecules between the two phases remained approximately 200, indicating a mixed solid–liquid system where the formed hydrate was incomplete and always presented liquid water.

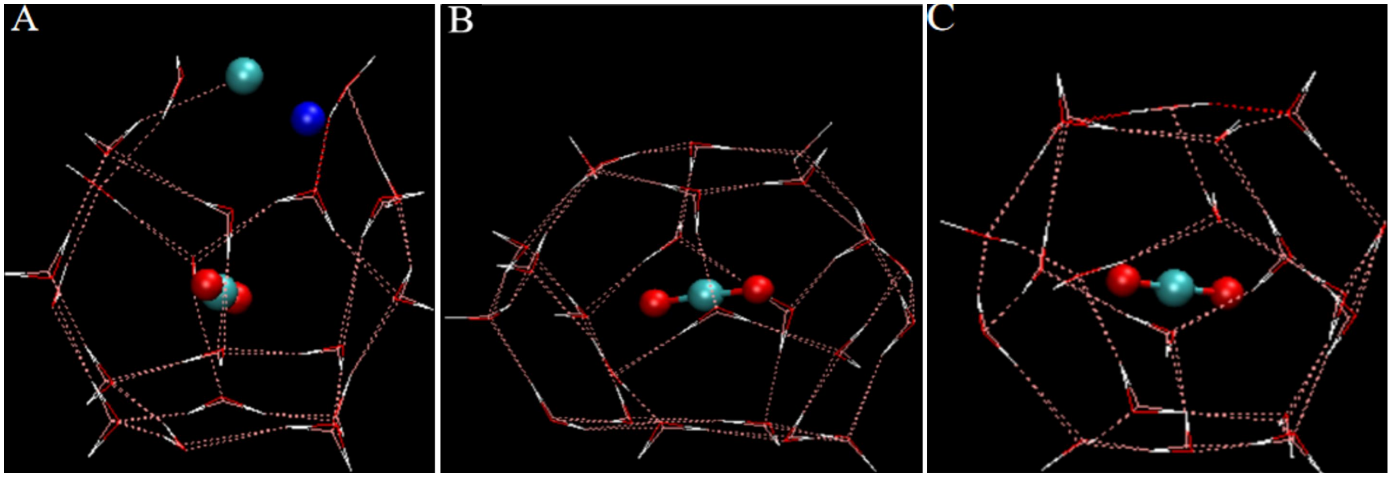

Figure 6
Single hydrate cage analysis, showing (A) an incomplete hydrate cage, (B) a perfect $5^{12}6^2$ hydrate cage and (C) a perfect 5^{12} hydrate cage.

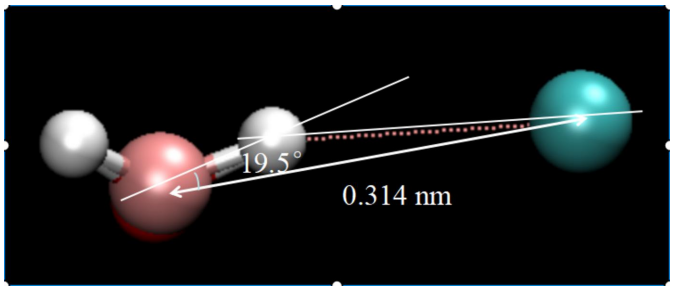

Figure 7
A typical hydrogen bond between a water molecule and Cl^-.

The density changes in the simulation system allow us to determine the growth of CO_2 hydrate (Fig. 5). It can be observed that the density underwent a significant rise from 0 to 400 ns and then approached a state of equilibrium. This indicates the formation of CO_2 hydrate. Once the CO_2 hydrate was formed, the density of the simulated system stabilized at approximately 1.133 g cm^{-3}. Considering that seawater typically has a density ranging from 1.02 to 1.07 g cm^{-3}, the generated CO_2 hydrate possessed a greater density than seawater, causing them to naturally settle downwards. These CO_2 hydrates can be safely stored in suitable locations on the seabed, such as deep saltwater layers, without being affected by ocean currents or other factors. This method effectively prevents secondary pollution resulting from CO_2 leakage.

3.4. Single hydrate cage analysis

In the above discussions, since the water molecules around Na^+ and Cl^- remain liquid, some of the water molecules cannot participate in the formation of a complete closed solid cage. In Fig. 6, specific hydrate cages are chosen for analysis. In Fig. 6(A), the pentagon forming the cage is disrupted due to the presence of Na^+ and Cl^-. The positively charged H atom in water is closer to the Cl^-, with the O atom and Cl^- being less than 3.5 Å apart, and the supplementary O—H···Cl angle being less than 35°, indicating the presence of a hydrogen bond, as shown in Fig. 7. Thus, it is believed that Cl^- contributes to the formation of the hydrate cage. However, the negatively charged O atoms in water are closer to Na^+, which being monatomic, does not form any bonds with the water molecules, preventing them from participating in closed cage formation; this is different to the report of Xu *et al.* (2021). In the region where there is no Na^+ and Cl^-, perfect cages can be seen. Fig. 6(B) depicts a complete $5^{12}6^2$ hydrate cage consisting of two opposing hexagons and 12 pentagons arranged to form a cage, and Fig. 6(C) depicts a complete 5^{12} hydrate cage, consisting of 12 pentagons arranged to form a cage. This cage effectively traps CO_2 and forms CO_2 hydrate.

4. Conclusions

Here are the main conclusions:

(1) During the simulation process, the presence of Na^+ and Cl^- was observed in the area where CO_2 defect hydrate forms. Analysis of a single cage revealed that the presence of Na^+ and Cl^- disrupted the pentagonal structure of the cage, resulting in an imperfect hydrate formation.

(2) In the growth process of CO_2 hydrate in brine, not all liquid water molecules participated in hydrate formation and there were always some liquid water molecules in the simulation box. The F3 and F4 order parameters indicated defects in the CO_2 hydrate within this system. Consequently, when carrying out carbon capture and storage in marine environments, the influence of salt ions should be taken into consideration.

(3) The density of the simulated system exhibited a significant increase within the 0–400 ns range and eventually reached equilibrium, indicating CO_2 hydrate generation. After a substantial number of hydrates were formed, the density of the simulated system stabilized at approximately 1.133 g cm^{-3}, which surpasses the average density of seawater. Consequently, the hydrate would naturally settle down. Suitable locations on the seabed, such as deep saltwater layers, can serve as stable storage sites for CO_2 hydrate.

Acknowledgements

The authors declare no conflicts of interest and that they have no known competing financial interests or personal relationships that may affect the work reported in this paper. All the data that support the findings of this study are available on request from the corresponding authors.

Funding information

Funding for this research was provided by: International Key Research and Development Plan (grant No. D2022YFF-0609702).

References

Abascal, J. L. F., Sanz, E., García Fernández, R. & Vega, C. (2005). *J. Chem. Phys.* **122**, 234511.
Abraham, M. J., Murtola, T., Schulz, R., Páll, S., Smith, J. C., Hess, B. & Lindahl, E. (2015). *SoftwareX*, **1–2**, 19–25.
Aminu, M. D., Nabavi, S. A., Rochelle, C. A. & Manovic, V. (2017). *Appl. Energy*, **208**, 1389–1419.
Arias, P., Bellouin, N., Coppola, E., Jones, R., Krinner, G., Marotzke, J., *et al.* (2021). *Climate Change 2021: The Physical Science Basis*. Contribution of Working Group I to the Sixth Assessment Report of the Intergovernmental Panel on Climate Change. The Intergovernmental Panel on Climate Change AR6. https://www.ipcc.ch/report/ar6/wg1/.
Aya, I., Yamane, K. & Nariai, H. (1997). *Energy*, **22**, 263–271.
Bussi, G., Donadio, D. & Parrinello, M. (2007). *J. Chem. Phys.* **126**, 014101.
Canadell, J. G., Meyer, C. P. M., Cook, G. D., Dowdy, A., Briggs, P. R., Knauer, J., Pepler, A. & Haverd, V. (2021). *Nat. Commun.* **12**, 6921.
Carretero-González, R., Kevrekidis, P. G., Kevrekidis, I. G., Maroudas, D. & Frantzeskakis, D. J. (2005). *Phys. Lett. A*, **341**, 128–134.
Dangendorf, S., Hendricks, N., Sun, Q., Klinck, J., Ezer, T., Frederikse, T., Calafat, F. M., Wahl, T. & Törnqvist, T. E. (2023). *Nat. Commun.* **14**, 1935.

Darden, T., York, D. & Pedersen, L. (1993). *J. Chem. Phys.* **98**, 10089–10092.
Faure-Schuyer, A., Welsch, M. & Pye, S. (2017). *Europe's Energy Transition*, edited by M. Welsch, S. Pye, D. Keles, A. Faure-Schuyer, A. Dobbins, A. Shivakumar, P. Deane & M. Howells, ch. 6, pp. 31–39, *European Energy Policy Objectives*. New York: Academic Press.
Harris, J. G. & Yung, K. H. (1995). *J. Phys. Chem.* **99**, 12021–12024.
He, Z., Linga, P. & Jiang, J. (2017). *Phys. Chem. Chem. Phys.* **19**, 15657–15661.
Hugonnet, R., McNabb, R., Berthier, E., Menounos, B., Nuth, C., Girod, L., Farinotti, D., Huss, M., Dussaillant, I., Brun, F. & Kääb, A. (2021). *Nature*, **592**, 726–731.
Humphrey, W., Dalke, A. & Schulten, K. (1996). *J. Mol. Graph.* **14**, 33–38.
Izquierdo-Ruiz, F., Otero-de-la-Roza, A., Contreras-García, J., Prieto-Ballesteros, O. & Recio, J. M. (2016). *Materials*, **9**, 777.
Jing, X., Luo, Q., Cui, X., Wang, Q., Liu, Y. & Fu, Z. (2022). *J. Mol. Liq.* **366**, 120237.
Kirchner, M. T., Boese, R., Billups, W. E. & Norman, L. R. (2004). *J. Am. Chem. Soc.* **126**, 9407–9412.
Koh, C. A. (2002). *Chem. Soc. Rev.* **31**, 157–167.
Lu, T. & Chen, F. (2012). *J. Comput. Chem.* **33**, 580–592.
McGlade, C. & Ekins, P. (2015). *Nature*, **517**, 187–190.
Nakate, P., Ghosh, B., Das, S., Roy, S. & Kumar, R. (2019). *Chin. J. Chem. Eng.* **27**, 2074–2080.
Nguyen, A. H. & Molinero, V. (2015). *J. Phys. Chem. B*, **119**, 9369–9376.
Raymond, C., Matthews, T. & Horton, R. M. (2020). *Sci. Adv.* **6**, eaaw1838.
Rogelj, J., den Elzen, M., Höhne, N., Fransen, T., Fekete, H., Winkler, H., Schaeffer, R., Sha, F., Riahi, K. & Meinshausen, M. (2016). *Nature*, **534**, 631–639.
Turgut, O., Bjerketvedt, V. S., Tomasgard, A. & Roussanaly, S. (2021). *J. Clean. Prod.* **329**, 129427.
Van Der Spoel, D., Lindahl, E., Hess, B., Groenhof, G., Mark, A. E. & Berendsen, H. J. C. (2005). *J. Comput. Chem.* **26**, 1701–1718.
Viebahn, P., Vallentin, D. & Höller, S. (2015). *Appl. Energy*, **157**, 229–244.
Walsh, M. R., Koh, C. A., Sloan, E. D., Sum, A. K. & Wu, D. T. (2009). *Science*, **326**, 1095–1098.
Wang, J. & Yan, Z. (2021). *Weather Clim. Extremes*, **34**, 100379.
Xu, J., Du, S., Hao, Y., Yang, X. & Zhang, J. (2021). *Chem. Phys.* **551**, 111323.
Zhang, Y., Zhao, L., Deng, S., Nie, X. & Du, Z. (2019). *Energy Procedia*, **158**, 4648–4654.
Zheng, J., Chong, Z. R., Qureshi, M. F. & Linga, P. (2020). *Energy Fuels*, **34**, 10529–10546.